

Calibration of a Long-Wavelength Acoustic Flowmeter Using a Lumped Impedance Acoustic Model

Lee J. Gorny
Keith A. Gillis
Michael R. Moldover
Sensor Science Division, National Institute of Standards and Technology (NIST)
100 Bureau Dr.
Gaithersburg
MD 20899
leeg@nist.gov

ABSTRACT

We are developing a long-wavelength acoustic flowmeter (LWAF) for accurate measurement of flue gas flows in, for example, coal-burning power plants. A LWAF is advantageous because it averages spatial non-uniformities in a flow's axial flow profile over the entire cross-section of the flue. We constructed a 1:100 scale, calibrated flow facility to evaluate long wavelength techniques. Using a prototype LWAF, we obtained an uncertainty of 1 % for flows ranging from 2 m/s to 5 m/s. We present our design considerations, the operating principles and numerical theory for the prototype LWAF, methods for its calibration, and measurement results taken in several distorted flows. In this discussion, we identify problems that must be solved to scale up the LWAF for deployment in a power-plant's stack.

1. INTRODUCTION

Because coal is heterogeneous, it is impractical to accurately quantify the CO₂ (and other greenhouse gases) emitted by a coal-burning power plant by weighing the coal burned. Instead, emissions are determined by measuring the mass flow and the composition of the flue gases in the plant's stack. Accurate measurements of mass flow in stacks using conventional flow measurement techniques¹ are difficult because the flow profile is poorly known and the flow measurements are made only in a limited volume (*e.g.* along a few chords sampled by conventional ultrasonic flow meters). During the mid-1970's, Robertson and Potzick^{2,3,4} studied an alternative to conventional flow measurement techniques: long-wavelength acoustic flowmeters (LWAF). Conceptually, they measured flows by monitoring propagation of acoustic plane waves in a duct. In contrast to conventional methods, a LWAF determined average flow across the duct's entire cross section.

Here, we reexamine LWAF techniques employing advances in signal processing, flow modeling, and sensor technology that have occurred since the 1970s. We built a calibrated 1:100 scale (0.1 m diameter) flow facility described in Section 2. Using it, we compare three frequency-domain LWAF techniques in Section 3. We derive a model for the acoustic pressure in the LWAF based on Crandall's transmission line theory for circular waveguides. Section 4 compares modeled data with LWAF measurements without flow, and presents a method to calibrate the LWAF's transducers. Once calibrated, we present uncertainties of LWAF measurements for velocities up to 5 m/s (0.047 kg/s) in Section 5. Our LWAF currently

measures flows with uncertainty less than 1 % in distorted swirling flow. (Unless otherwise specified, uncertainties are one standard uncertainty corresponding to a 68 % confidence level.)

2. THE 1:100 SCALE STACK SIMULATING LWAF TESTBED

We developed a facility to evaluate the LWAF's ability to measure the speed of sound and flowrate of a distorted flow. It is comprised of four primary sections as shown in Figure 1. An inlet section (1) provides a uniform, undistorted flow into a calibrated laminar flow meter (LFM) (2) that measures flow with a relative uncertainty of 0.2 %. A 2-axis, out-of-plane, return bend (3) generates a swirling flow into the LWAF (4). The LWAF is comprised of a loudspeaker array, a microphone array, and an easily adjustable outlet length. We note that flue-gas flows in coal-burning plants reach 12 m/s (in brick-lined concrete stacks) and 20 m/s (in borosilicate glass-lined stacks). We are constructing a facility capable of generating flows up to 30 m/s, but the data here are limited to 5 m/s.

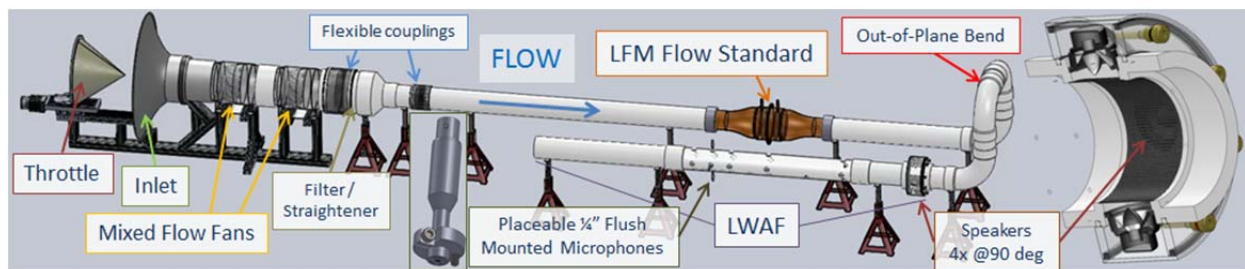


Figure 1: Diagram of the LWAF evaluation facility.

Relevant flow parameters to an LWAF's operation are the Mach Number, Reynolds Number, cut-on-frequency and speed of sound, defined respectively as: $Ma = V/c$, $Re = \rho V D / \mu$, $f_{co} = 1.841c / (\pi D)$ and $c = (\rho \kappa_s)^{-1/2}$. Here ρ is the density of the gas, μ is the dynamic (shear) viscosity, V is the average linear flow velocity, D is the diameter of the duct, and κ_s is the adiabatic compressibility of the gas. Reference 4 shows that flow-generated distortions result in propagation uncertainties of an acoustic plane wave on the order of Ma^2 . In stacks, $Ma < 0.06$; therefore, corrections on the order of Ma^2 are small. However, power plant stack flows are highly turbulent with Re in the range $10^6 < Re < 10^8$. Blower-generated and turbulence-generated noise [which scale as $(Re)^6$ and $(Re)^8$ respectively]⁶ are prominent. The f_{co} is the frequency below which only plane waves will propagate within a duct. For a 10 m diameter stack $f_{co} \approx 20$ Hz, the low frequency threshold of human hearing.

Our facility has a $f_{co} \approx 2$ kHz with measurement sections comprised primarily of $D \approx 0.102$ m (4 inch) diameter, schedule 40, polyvinyl chloride (PVC) pipe. A fully developed, undistorted flow is encouraged through the LFM with 15 and 7.5 diameters of straight pipe upstream and downstream, respectively. The facility's outlet is an un-flanged circular pipe, similar to a stack's liner. Downstream propagating acoustic waves in the pipe are partially radiated from the opening and partially reflected back upstream at the open end resulting in a standing wave pattern. Reflected waves from upstream components contribute to the standing wave pattern as outgoing pressure propagations.

There are 24 total mounting holes in the 1 m measurement section that house microphones and other sensors. Holes are staggered axially at (0.05, 0.10 and 0.20) m and circumferentially at 90 degrees. Figure 2a shows a schematic of our LWAF. Each of the seven microphones in the

facility is given a number, denoted as M for microphone followed by its number. We generate plane sound waves using 4 loudspeakers positioned in a circumferential array (as shown as a cutaway view to the right of Figure 1). The driven acoustic waves are either pulsed (for time-of-flight measurements) or continuous (for standing wave measurements) as shown in Figure 2b.

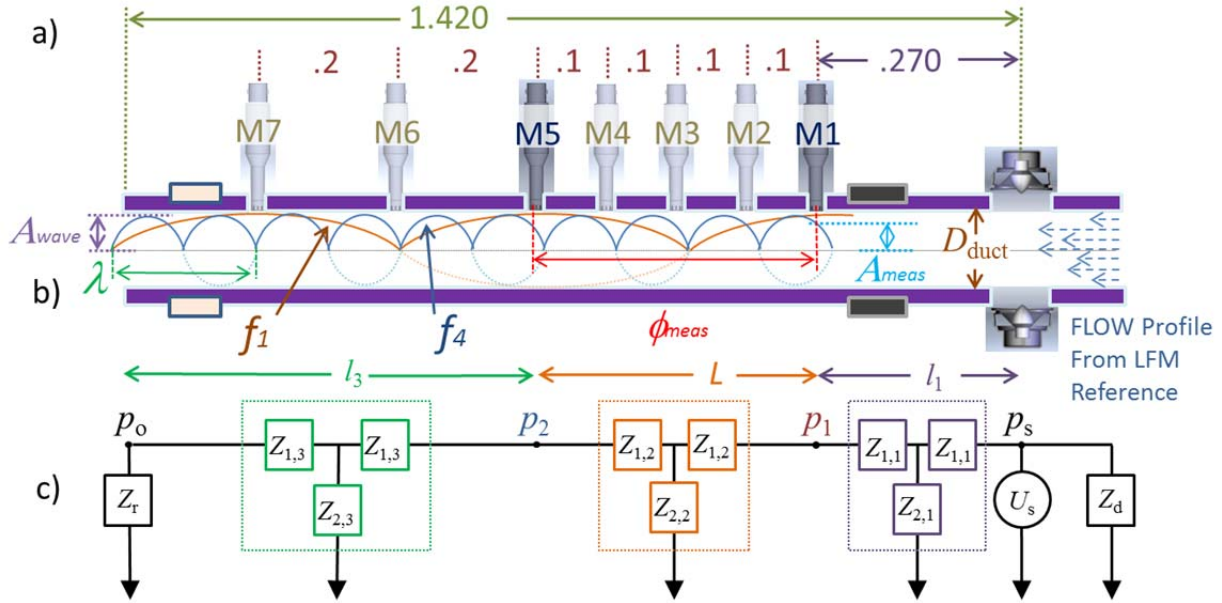


Figure 2: Schematic of the LWAF geometry. (a) Nominal dimensions (in meters) (b) Standing waves f_1 and f_4 tuned with multiples of one-half-wavelength between paired M5 and M1 (c) An equivalent circuit schematic to the LWAF.

We use LabView⁹ to communicate with instruments, measure data and to control flow through the facility. We measure the absolute static pressure (P) at the LWAF and LFM, the differential pressure (DP) across the LFM, the temperature (T) upstream and downstream of the LFM, within the LWAF and in the room and relative humidity (RH) to approximate the composition of air passing through the facility. Each of the 7, 6.3 mm (1/4 inch), free-field electret microphones is calibrated at room temperature from 0 kHz to 5 kHz. Further details about the facility and this process can be found in our publication for the 2012 CEESI ISFFM conference.⁷

3. THE LWAF AND ITS LUMPED IMPEDANCE CALIBRATION MODEL

We determine the speed of sound (c) and average flow velocity (V) through the LWAF by driving the loudspeaker array continuously across a range of frequencies and measuring the amplitude and phase of the pressure detected by each microphone. Section 3A describes how the acoustic pressure can be used to determine c and V . Because each microphone's response is not identical, and their relative spacing along the duct is not precisely known, it becomes necessary to calibrate microphones for accurate measurements. We determine spacing experimentally by aligning the experimental acoustic pressure measurements made when no flow is present. Relative sensitivity calibration of microphone pairs can be measured experimentally using a G.R.A.S Sound & Vibration Type 51AB Sound Intensity Calibrator.⁹ Calibration can be performed numerically by aligning the no flow measured pressure response with a response calculated using a transmission line theory model which we derive in Section 3B. The two methods are compared in Section 5, illustrating that improved accuracy can be achieved using numerical calibration. Figure 3 illustrates the differences between calibrated and un-calibrated pressure response data.

A. Determining Speed of Sound and Average Flow Velocity using a LWAF

Standing wave patterns emerge if the loudspeaker drives continuous (or semi-continuous using a swept sine function) acoustic waves between the loudspeaker and open end of the duct. The frequency response function FRF allows us to characterize standing waves across a range of frequencies where only long wavelength waves exist. FRF is plotted in Figure 3 as magnitude $A = p_5 / p_1$ and phase $\phi = \phi_5 - \phi_1$ components as a function of fL , where f is the frequency and L is the distance between the microphones.

Using the FRF, we measure c and V in three ways. From the FRF plots, and Figure 2b, one can see that for specific wavelengths λ_n , as in cases f_1 and f_4 , have $\lambda_n = 2L/n$ where n is the number of $1/2$ wavelengths between microphones. f_n can be found from the FRF magnitude plot as locations where $A = 1$ (referred to here as the “mag sel” method) or where FRF phase is tangent to its linear interpolation (“phs sel”) as shown in Figure 3c. At these frequencies, the LWAF’s response is evaluated to obtain

$$c = 2f_n L/n, \text{ and } Ma = V/c = \Delta\phi_n / (n\pi) = \omega_n \Delta t / (n\pi) \quad (1,2)$$

where $\Delta\phi_n = \phi_{\text{flow}} - \phi_{\text{no flow}}$ and $\phi_{\text{no flow}} = \pi n$, where $\phi_{\text{no flow}}$ is measured in radians.⁴ A third “slope” method determines $c + V = 2\pi L / \partial\phi / \partial f$ from the phase change across the entire frequency range as shown in Figure 3b, and c is determined using Equation (1) or from NIST’s Reference Fluid Thermodynamic and Transport Properties Database (REFPROP) v9.0.¹¹ We are investigating the use of resonance and anti-resonance frequencies of the ducted geometry to independently measure c . Details about these calculations and their implementation in the LWAF can be found in our prior work⁷ and will be discussed in a forthcoming publication.

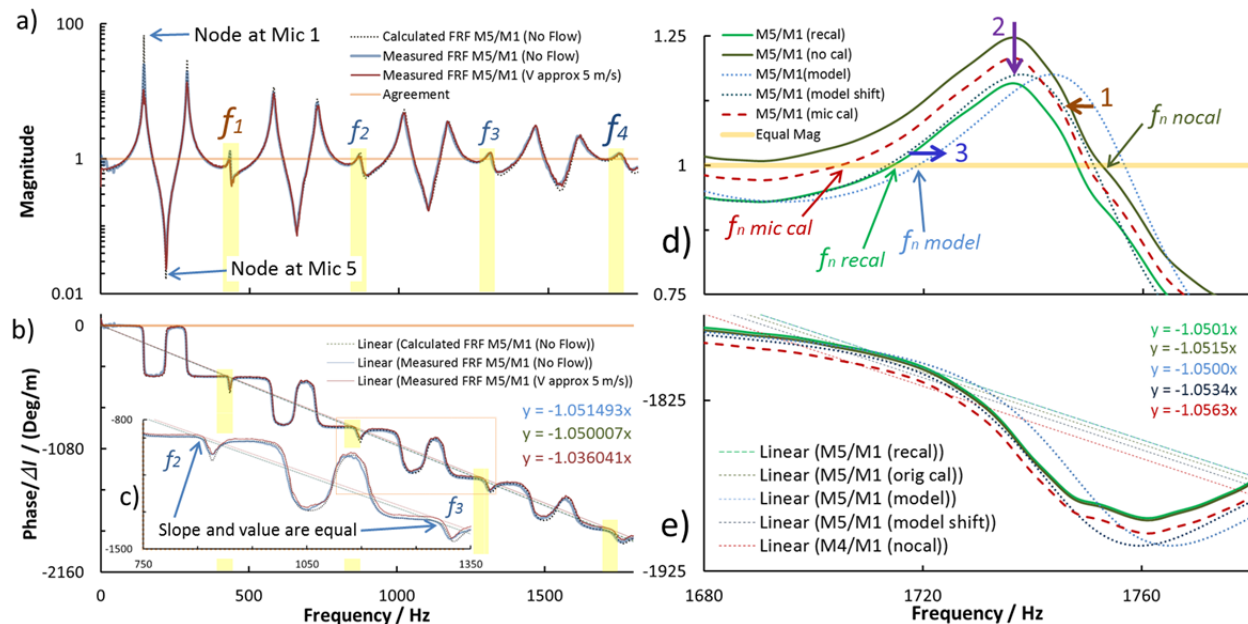


Figure 3: The calculated and measured FRF magnitude and phase (a) and (b) are shown for cases with and without flow. Highlighted regions illustrate f_n where $1/2$ wavelength multiples exist. The expanded FRF phase plot (c) shows the relationship between the linear interpolation and measured phase. Three modifications allow us to calibrate the M4/M1 microphone pair. The FRF (d) magnitude and (e) phase illustrate each step.

B. Development of a Lumped Impedance Model for $V = 0$

Our model assumes plane wave propagation with $e^{i\omega t}$ time-dependence for the acoustic pressure p and acoustic volume velocity U in the absence of flow. Figure 2c shows an equivalent circuit to our LWAF for microphone pair M5/M1. It is comprised of three T-networks (shown as three colored boxes) that model waveguide sections l_1 , L , and l_3 . These sections are used to calculate the acoustic pressure at each microphone. An impedance Z_r models the radiation impedance from the open end. Speakers are modeled as a volume velocity source U_s and upstream ductwork is given an impedance Z_d .¹² We neglect the admittance of the microphones, and assume rigid walls of uniform cross section.

Each T-network contains impedances $Z_{1,i}$ and $Z_{2,i}$ that model the propagation of sound over that length of duct. Crandall shows that long wavelength sound propagation is analogous to electromagnetic wave propagation in a lossy transmission line, where acoustic pressure p corresponds to voltage and the acoustic volume velocity U to current.¹³ The p and U at axial position x are described by the coupled differential equations

$$\frac{\partial p}{\partial x} = -\mathcal{Z}U \quad \text{and} \quad \frac{\partial U}{\partial x} = -\mathcal{Y}p, \quad (3,4)$$

$$\text{where } \mathcal{Z} = \frac{i\omega\rho}{A} \frac{1}{1-F_\eta}, \quad \mathcal{Y} = \frac{i\omega A}{\rho c^2} [1 + (\gamma-1)F_\kappa] \quad \text{and} \quad F_\kappa = \frac{2J_1(\zeta_\kappa)}{\zeta_\kappa J_0(\zeta_\kappa)}. \quad (5,6,7)$$

The series impedance per unit length \mathcal{Z} and the parallel admittance per unit length \mathcal{Y} account for the viscous damping effects from interaction and thermal diffusion respectively with the wall. F_κ is the thermal loss function. J_0 and J_1 are Bessel functions of order 0 and 1, respectively; $\zeta_\kappa \equiv (1-i)r/\delta_\kappa$; and $\delta_\kappa = \sqrt{2D_\kappa/\omega}$ is the thermal penetration length. Here, the thermal diffusivity $D_\kappa = \kappa_T/\rho C_p$. The viscous loss function F_η has the same functional form as (7) but with the viscous penetration length $\delta_\eta = \sqrt{2\eta/\rho\omega} = \sqrt{\text{Pr}} \delta_\kappa$ instead of δ_κ . The acoustic pressure and volume velocity for plane waves traveling in the $\pm x$ direction are proportional to $\exp(\mp\Gamma x + i\omega t)$ where Γ is the propagation parameter, given by

$$\Gamma = \sqrt{\mathcal{Z}\mathcal{Y}} = \frac{i\omega}{c} \sqrt{\frac{1 + (\gamma-1)F_\kappa}{1 - F_\eta}}. \quad (8)$$

Substituting into Equations (3 and 4) we find the ratios p_+/U_+ , p_-/U_- and the characteristic impedance

$$Z_0 = \sqrt{\mathcal{Z}/\mathcal{Y}} = \frac{\rho c}{A} \frac{1}{\sqrt{[1 + (\gamma-1)F_\kappa](1 - F_\eta)}}. \quad (9)$$

In terms of these defined quantities, the lumped elements $Z_{1,i}$ and $Z_{2,i}$, for a circular duct with length l_i and cross sectional area $A = \pi r^2$, are given by

$$Z_{1,i} = Z_0 \tanh\left(\frac{1}{2}\Gamma l_i\right) = \frac{i\omega\rho l_i}{2A(1-F_\eta)} \frac{\tanh\left(\frac{1}{2}\Gamma l_i\right)}{\frac{1}{2}\Gamma l_i}, \quad \text{and} \quad (10)$$

$$Z_{2,i} = \frac{Z_0}{\sinh(\Gamma l_i)} = \frac{\rho c^2}{i\omega A l_i [1 + (\gamma - 1) F_\kappa]} \frac{\Gamma l_i}{\sinh(\Gamma l_i)} \quad (11)$$

In the rightmost sides of Equations (10) and (11), the ratios of the hyperbolic functions to their arguments approach unity in the long wavelength limit $kl_i \ll 1$.

Referring to Figure 2c, the i th section has length l_i and impedances $Z_{1,i}$ and $Z_{2,i}$ subscripted to distinguish them. However, since D is constant, Γ and Z_0 are identical. The input impedance of a single T-network, representing a duct of length l_i , terminated with impedance Z_{load} is given by

$$Z_{in} = Z_0 \frac{Z_{load} + Z_0 \tanh(\Gamma l_i)}{Z_0 + Z_{load} \tanh(\Gamma l_i)}. \quad (12)$$

The ratio of the acoustic pressure at the input to the pressure at the load is

$$\frac{p_{in}}{p_{load}} = \frac{Z_{in}}{Z_{load}} \left[1 + \frac{Z_{load}}{Z_0} \tanh(\Gamma l_i) \right] \cosh(\Gamma l_i). \quad (13)$$

When we apply these formulas to the circuit in Figure 2c, we obtain the pressure ratio

$$\frac{p_1}{p_2} = \frac{Z_{in2}}{Z_{in3}} \left[1 + \frac{Z_{in3}}{Z_0} \tanh(\Gamma L) \right] \cosh(\Gamma L), \text{ where} \quad (14)$$

$$Z_{in2} = Z_0 \frac{Z_{in3} + Z_0 \tanh(\Gamma L)}{Z_0 + Z_{in3} \tanh(\Gamma L)} \text{ and } Z_{in3} = Z_0 \frac{Z_r + Z_0 \tanh(\Gamma l_3)}{Z_0 + Z_r \tanh(\Gamma l_3)} \quad (15, 16)$$

After substitution and simplification, we get our FRF modeling equation

$$\frac{p_2}{p_1} = \frac{(Z_r/Z_0) \cosh(\Gamma l_3) + \sinh(\Gamma l_3)}{(Z_r/Z_0) \cosh[\Gamma(L+l_3)] + \sinh[\Gamma(L+l_3)]}. \quad (17)$$

Levine and Schwinger (L&S), calculated the reflection coefficient, neglecting thermoviscous dissipation, for acoustic waves in a semi-infinite circular duct (radius a) exiting an unflanged open end into free space.¹⁴ Rigorous formal expressions were derived for the magnitude of the reflection coefficient $|R|$ and the effective length correction l/a , using their notation. Here, we use approximations to L&S's calculations using notation consistent with earlier reports and publications by NIST's Fluid Metrology Group.¹⁵

4. MODEL COMPARISON WITH MEASURED DATA AND LWAF CALIBRATION

Using the transmission line theory model from Section 3B, we calculate a frequency response function (FRF) for each microphone pair in our LWAF using Equation 17. Measurements of T , P , and RH allow us to determine approximate air composition, and c for the model c_m . Figure 3 shows a comparison of the modeled FRF with a measurement for pair M5/M1. The model generally has larger peaks indicating a shortcoming in our standing wave ratio calculation. However, the shape of the calculated FRF provides enough information to calibrate microphone pairs by aligning the two FRFs. With the model, we no longer need to use our intensity probe calibrator, eliminating the need to remove microphones from the LWAF in calibration. Instead we numerically calibrate pairs in situ with improved accuracy.

Figures 3d and 3e illustrate the steps we took to numerically calibrate our facility. Calibration of the LWAF has three steps: The un-calibrated “no cal” and modeled “model” FRFs are not aligned along either the x or y axes of Figure 3d. Deviations along the x-axis arise from uncertainty in c_m with respect to the actual c or because of microphone spacing (L) inconsistency. To correct this, we adjust the binwidth of the model data, align peaks and valleys with the measurement. This results in the “model shift” FRF (1). Amplitude is modified by subtracting the “no cal” data from the “model shift” to obtain a calibration curve. The curve is smoothed and added to the “no cal” data resulting in the “recal” FRF (2). The “recal” and “model” FRF phase plots then have nearly identical slopes indicating their agreement. Last, (3) we determine spacing using the relationship $c = 2f_n L/n$ to get $L_{LWAF} = f_{n_model} L_{model} / f_{n_recal}$ (ie. setting the modeled and experimental c as equal). L_{LWAF} is the model calibrated microphone spacing. Figure 3d shows that the difference in f_n between calibrations can be significant. No flow calibration of the LWAF at a known speed of sound allows for greater accuracy in subsequent measurements. Even using a poorly aligned f_n such as the initial “mic cal” FRF, we can measure of c relatively accurately because the FRF magnitude is independent of flow and FRF phase changes proportionally to flow.

5. RESULTS OF THE CALIBRATED LWAF

Figure 4 presents LWAF results from 740, 60 s data sets taken under varying flow conditions. Data are grouped into nominal V and c ranges by each set’s LFM and REFPROP reference values. The “slope” and “phs sel” method’s data are shifted to the left and right of the average value for clarity. We used the data set for both plots, only changing the calibration. Figures 4a and 4c use the intensity probe calibrator and Figures 4b and 4d, the transmission line theory based model. Results are similar, partially because of the no-flow calibration of the meter. If the sets are not corrected at no-flow, the modeled data set has much less deviation although errors for some measurements are significantly larger than 2.5 % for V . This result illustrates that a LWAF can be calibrated in situ using our numerical model.

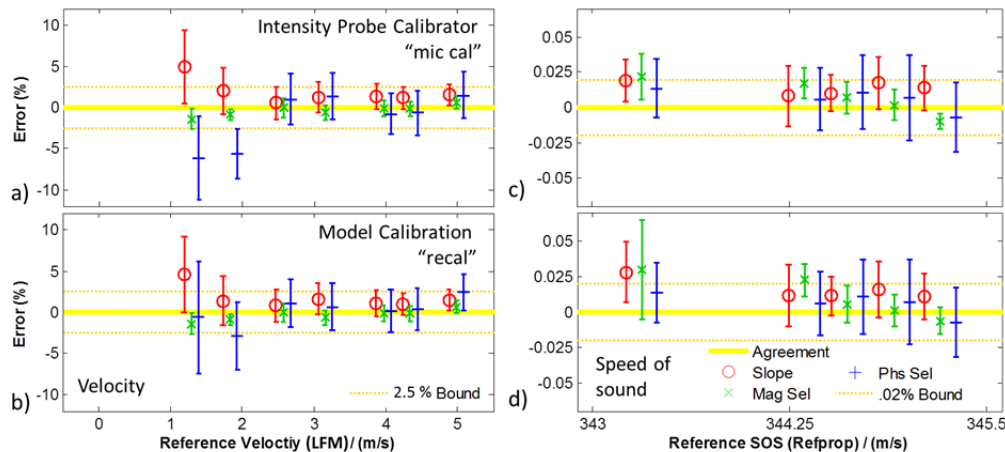


Figure 4: Error in measurement of V and c using an intensity probe calibrator (a, c) vs. model calibration (b, d).

An additional improvement in data processing is made after calibration by including averaging of several FRF generated from each 60 s time series. Data in Figure 4 uses a single FRF for each time series resulting in a well averaged FRF, with potential inaccuracies in determining f_n due to curve fitting and round off errors. Instead, we break up the 60 second interval into 6, 30 s intervals staggered by 5 s (ie. 0 s to 30 s, 5 s to 35 s, etc.). We can then average 6 FRF

measurements, rejecting significant outliers and report more accurate results. Data shown in Figure 5 for V and c are calculated using this averaging method. Measured velocity agrees with the reference flowmeter to within 1% for flows ranging from 2 m/s to 5 m/s.

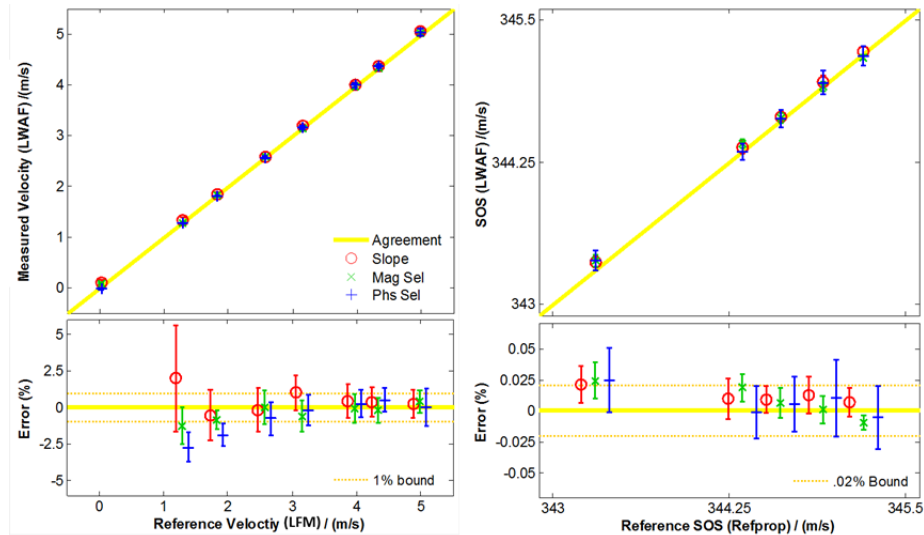


Figure 5: Flow measurement of V and c with intensity probe calibration and FRF averaging.

6. CONCLUSIONS

Frequency based V and c measurements have a standard deviation of approximately 1% and 0.02% for flows between 2 m/s and 5 m/s in distorted flow. This work shows progress toward the project's ultimate goal of obtaining uncertainties better than 1% uncertainty in measuring 2 m/s to 30 m/s flows. We have been able to accomplish this using averaging several shorter FRF measurements. Care must be taken to achieve a balance between collecting enough samples that noise is removed in each FRF while having enough samples to average. At low flow, one must determine c with accuracy greater than 0.02% to determine V with 1% uncertainty.

We developed a numerical model to calculate the flow free frequency response within our LWAF. It was used to calibrate our microphones with similar, slightly better results than were achieved with an intensity probe calibrator. Results are improved more substantially if the flowmeter is not calibrated at no-flow. The next step will be to incorporate flow into our numerical model. Then we could integrate modeled data into the LWAF calculation process, allowing for faster, more accurate determination of flow parameters and rapid localization of f_n .

We are currently constructing a larger scale facility with a maximum flow through the LWAF of 32 m/s. We will further evaluate the robustness of the LWAF using turbulence generators, in cases with increased swirl, and we will assess the influence of obstructions in the flow. Ultimately, our goal is to progress LWAF techniques to a point where they will be useable at a full scale power plant, arriving at a method that provides a lower cost, more accurate alternative for measuring power plant exhaust flows.

ACKNOWLEDGEMENTS

The authors would like to thank the NIST Greenhouse Gas and Climate Science Measurements Program and Michael Zachariah at the University of Maryland for their generous support of this research. Aaron Johnson and Gina Kline in Fluid Metrology Group calibrated the LFM used for these experiments and we are grateful for their assistance and expertise.

REFERENCES

1. S.K. Norfleet, M.R. O'Connell, "What's Everyone Using? Part 75 CEMS Equipment Trends - 2012 Update," *EPRI CEMS Users Group Meeting*, May 9-10 (2012).
2. B. Robertson, "Effect of Arbitrary Temperature and Flow Profiles on the Speed of Sound in a Pipe," *J. Acoust. Soc. Am.*, **62(4)**, pp. 813-818 (1977).
3. J.E. Potzick and B. Robertson, "Long-Wave Acoustic Flowmeter," *ISA Transactions*, **22(3)**, pp. 9-15, (1983).
4. J.E. Potzick and B. Robertson, "Long Wavelength Acoustic Flowmeter," *United States Patent* 4,445,389. (1984)
5. D.K. Anderson and L.A. Maroti, "Designing Wet Duct/Stack Systems for Coal-Fired Power Plants," *Power Magazine*, March, 15 (2006).
6. M.J. Lighthill, "On Sound Generated Aerodynamically. I General Theory," *Proc. R. Soc. Lond. A* **20 vol. 211, no. 1108**, pp. 564-587, (1952).
7. L.J. Gorny, K.A. Gillis, M.R. Moldover, "Testing Long-Wavelength Acoustic Flowmeter Concepts for Flue Gas Flows," *Proceedings of the 8th international Symposium for Fluid Flow Measurement* (2012).
8. J.D. Wright and A.N. Johnson, "NIST Lowers Gas Flow Uncertainties to 0.025% or Less," *NCSL International Measure*, **Vol. 5**, pp. 30-39, (2010).
9. In order to describe materials and experimental procedures adequately, it is occasionally necessary to identify commercial products by the manufacturer's name or label. In no instance does such identification imply endorsement by the National Institute of Standards and Technology, nor does it imply that the particular product or equipment is necessarily the best available for the purpose.
10. Reduced from NOAA Earth System Research Laboratory (2012) *data obtained via Wikipedia*.
11. E.W. Lemmon, M.L. Huber and M.O. McLinden, "NIST Standard Reference Data Base 23: Reference Fluid Thermodynamic and Transport Properties, Version 9.0," *National Institute for Standards and Technology, Standard Reference Data Program*, Gaithersburg, MD, (2010).
12. O. K. Mawardi, "On the propagation of sound waves in narrow conduits," *J. Acoust. Soc. Am.* **Vol. 21**, pp. 482-486 (1949).
13. I. B. Crandall, *Theory of Vibrating Systems and Sound* (Van Nostrand, New York, 1927), pp. 229-241.
14. H. Levine, "On the radiation of sound from an unflanged circular pipe," *Phys Rev* **73**, 383 (1948).
15. K.A. Gillis, J.B. Mehl, M.R. Moldover, "Theory of the Greenspan viscometer," *J. Acoust. Soc. Am.* **Vol. 114, Issue 1**, pp. 166-173 (2003).